Journal of Bionic Engineering
https://doi.org/10.1007/s42235-023-00428-9

RESEARCH ARTICLE

A Miniaturized Crawler Design Based on an Origami-inspired and Geometrically Constrained Spherical Six-bar Linkage

Subin Chae[1] · **Gwang-Pil Jung**[1]

Received: 29 May 2023 / Revised: 3 August 2023 / Accepted: 8 August 2023

Abstract
This paper focuses on a newly developed transmission for a milli-scale eight-legged crawling robot called OriSCO. The transmission allows intuitive steering by directly changing the direction of the propulsion force. The transmission is based on the constrained spherical six-bar linkage. The constrained spherical six-bar linkage passes only reciprocating motion out of the motor's rotating motion, allowing the crawling legs to kick the ground and obtain propulsion. Steering is achieved by adjusting the geometric constraints of the spherical six-bar using a servomotor, allowing the direction of propulsion to be changed. As a result, the OriSCO can move along the ground at a speed of 2.15 body lengths/s, and the robot is 60 mm long.

Keywords Bio-inspired robot · Crawler · Crawling robot · Direction change · Spherical six-bar linkage

1 Introduction

Small legged robots have been widely studied due to their advantages in certain conditions; they can traverse fine gaps as well as maneuver meager spaces, which large robots can hardly accomplish [1]. Legged robots can travel competently on the ground, whether it is level, rough, or even unpaved [2, 3]. Owing to the advantages of legged robots, they have been invented for exploration, reconnaissance, and so on [4–6].

To utilize the advantages of small legged crawling robots, several platforms have been developed to date [7–18]. Commonly these crawlers have focused on satisfying two requirements: lift and swing motion, and steering [19]. To achieve the lift and swing motion, a variety of transmissions such as four-bar oar mechanisms and spherical five-bar linkages are proposed. In the case of the steering, most of the crawling platforms use a similar steering method. They generate unbalanced moments on the body by controlling each leg's velocity, stride and moving direction, allowing the platforms to change the heading direction, or, some of the crawlers may require a certain gait pattern in order to achieve steering [20].

✉ Gwang-Pil Jung
gpjung@seoultech.ac.kr

[1] Department of Mechanical and Automotive Engineering, Seoul National University of Science and Technology, Seoul 01811, South Korea

For example, Hoover et al. [7], Haldane et al. [8], and Pullin et al. [9] use origami four-bar linkages. The different stride frequency of the left and right legs gives the platforms steer. An orthogonal 4-bar transmission is applied for a myriapod millirobot made by Hoffman et al. [10], which uses two pairs of piezoelectric bimorph actuators and controls the frequency for the steering. Baisch et al. [11] suggest the use of a two-DoF flexure-based spherical five-bar mechanism for each of its hip joints. It achieves steering by adjusting the frequency of each actuator. Soltero et al. [12] use two servo motors, orthogonal to each other, for each leg, a total of twelve servo motors, which can let the leg lift and swing. It uses two methods for the steering, making different actuation directions of each side and differentiating the stride of one side. Kim et al. [13] use an independent DC motor on each side, and it achieves steering motion by controlling the motors separately. Lee et al. [14] manipulate its legs through a crank-slider mechanism, and its steering motion is done by the differential drive of the two motors. Birkmeyer et al. [15] use a different steering method. It achieves steering by distorting the whole body structure using a Shape Memory Alloy (SMA) wire. The wire changes the leg arrangement and accordingly, the heading direction is altered as well.

The crawling platforms mentioned above have shown successful performance. However, there is still room for a more intuitive method of steering. The current steering method uses friction difference between the legs on each side. This friction differs depending on the stride frequency of the legs

Published online: 08 September 2023

on each side and causes unbalanced moments on the body. But, the friction between the legs and ground is not always regular, even if a crawler gets a constant speed command. The contact between the legs and ground occurs randomly; accordingly, the cralwer's orientation is irregularly affected. For example, a crawler is hard to follow a straight line even when the legs on each side operate at an equal speed. To assure the proceeding orientation, a closed-loop control is essential [17] and the control cost increases as the clawer wants to go faster.

In order to solve this fundamental issue, in this paper, we propose an intuitive steering method by means of a novel transmission design that allows the crawling legs to directly adjust the direction of the propulsion force. The proposed transmission is demonstrated by building a compact and lightweight crawling octopod (OriSCO). The key working principles are the constrained spherical six-bar and active control of the geometric constraint of the spherical six-bar. The constrained spherical six-bar linkage works as a mechanical filter, allowing only reciprocating motion to pass from the rotary motion of the motor. This reciprocating motion allows the crawling legs to kick the ground and the crawling robot to gain propulsion. If we change the geometric constraints using a servomotor, the direction of the reciprocating motion will change. Accordingly, the propulsion force acts in that direction and eventually, the crawling robot changes its direction of travel. Based on these two key principles, the OriSCO successfully crawls at the maximum speed of 2.15 body lengths per second, and the steering is realized with a single servomotor by varying the geometric constraint with an average angular speed of 91.93 and 60.73 degrees per second, left and right, respectively.

The following sections describe the design, modeling, and experimental results. The design section describes how the motion of the motors is transmitted to the crawling legs and how steering is achieved. In the modeling section, the constrained spherical six-bar is kinematically modeled. The model is used to investigate the foot trajectory when the constrained angle of the spherical six-bar is changed, which is related to the steering ability of the crawler. To check the performance of the crawler, experiments such as straight crawling, steering, and reaction force measurement are carried out.

2 Design

The OriSCO transfers the rotating motion of the motor to the crawling legs. To get enough propulsion from the ground for successful crawling, the motor's rotary motion should be converted to reciprocating motion. This process is enabled by the constrained spherical six-bar located between the motor and the crawling legs, which will be explained shortly.

The other design goal is to give the OriSCO the ability to steer. To this end, the angle between the ground and the reciprocating direction of the crawling legs should be altered. This alternation is done by varying the geometric constraint of the spherical six-bar and ultimately produces a propulsion in a different direction, which enables the OriSCO to successfully achieve steering.

2.1 Crawling Mechanism

The overall design of the OriSCO is shown in Fig. 1. The OriSCO has two sets of four crawling legs. One set are the hind legs and the other set are the front legs. The front and hind legs have different roles when kicking the ground, as shown in Fig. 2. In Fig. 2c, the rear legs have been designed to provide propulsion for the robot to move forward. Figure 2d shows the snapshot taken by the high-speed camera. The rear legs allow OriSCO to move forward. The front legs are designed to lift the crawler as shown in Fig. 2a. Thanks to the lifting motion shown in Fig. 2b, the preceding legs do not interfere with the next crawling stage by imposing friction on the ground.

At the center of the crawler is the gearbox with two DC motors. One motor is for the front legs and the other is for the back legs. The gearbox generates the rotary motion, and

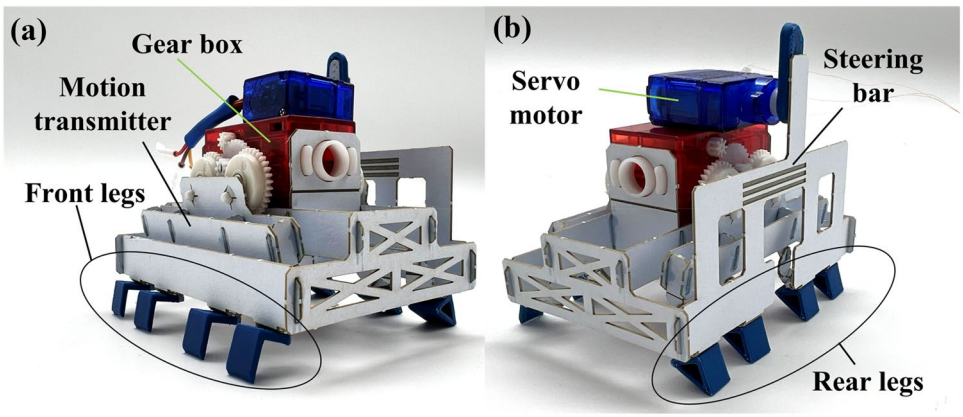

Fig. 1 A milli-scale crawler using a constrained spherical six-bar, viewed from (**a**) the left diagonal and (**b**) the right diagonal. The crawler has a size of 85 × 60 × 60 mm and a weight of 46.86 g

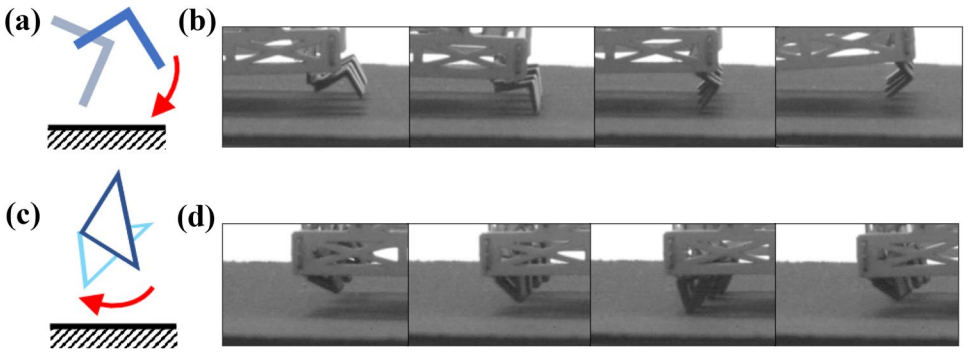

Fig. 2 The front leg concentrates on vertical movement as shown in **a** and **b**. The rear legs mainly provide propulsion through horizontal movement as shown in **c** and **d**

the motion is transmitted to the crawling legs through the motion transmitter shown in Fig. 1. To convert this rotary motion into the reciprocating motion for the crawling legs, a constrained spherical six-bar is used between the motor and the crawling legs. The spherical six-bar passes only the reciprocating motion out of the rotating motion of the motor. This is similar to the crank-slider linkage, but it requires conventional mechanical parts such as bearings, pins, and links, which may cause wear-related issues and increase in size and weight. On the other hand, the spherical six-bar linkage can be designed with a 2D origami pattern and fabricated using a method of smart composite microstructures (SCM) [21]. Due to these properties, it consists of several folding lines and facets, allowing the mechanism to be small and lightweight.

The spherical six-bar linkage is shown in Fig. 3. The six-bar pattern was designed to fold in a single direction by designing it in an anisotropic manner. If the front crease is thick and the back crease is thin, the pattern will fold only in the direction of the thicker crease. The spherical six-bar pattern has six facets, and all the facets meet at a vertex positioned in the center, and the vertex is the center of rotation, as shown in Fig. 3a. Two additional sides at the top and bottom edges enable the pattern to bring about the kicking motion. In Fig. 3b, c, the location of the spherical six-bar is shown. The spherical six-bar is located between the crawling legs and the motion transmitter. To construct the reciprocating motion using the pattern, the bottom edge of the bar is fixed to the body frame and the other side is connected to the motion transmitter so that it works like a crank-slider mechanism in a plan view.

The working process of the constrained spherical six-bar is shown in Fig. 4. The rotating motion is given using a tweezer in Fig. 4(a-1). If we focus on the facet for foot attachment, the facet reciprocates according to the yellow arrow shown in Fig. 4(a-2). Among the rotational motions, motions other than reciprocation are transferred to the side facets of the spherical six-bar. In other words, the constrained spherical six-bar works as a mechanical filter that passes only reciprocating motion [22].

Figure 5 shows the detailed process of how the rotating motion of the motor causes the rear crawling legs to reciprocate. Figure 5a shows that the crank is in the lowest position while the crawling leg is in the aerial phase. After the crank is turned 90 degrees clockwise, the crawling legs begin to kick as shown in Fig. 5b. In Fig. 5b, the lateral motion is transferred to the side facets and the spherical six-bar is asymmetrically folded. As a result, only up-and-down motion is shown in the crawling legs. Figure 5c is when the crank is in the top position and the crawling legs are kicking the ground at this time. After kicking the ground, the crawling legs are retracted by the crank rotation shown in

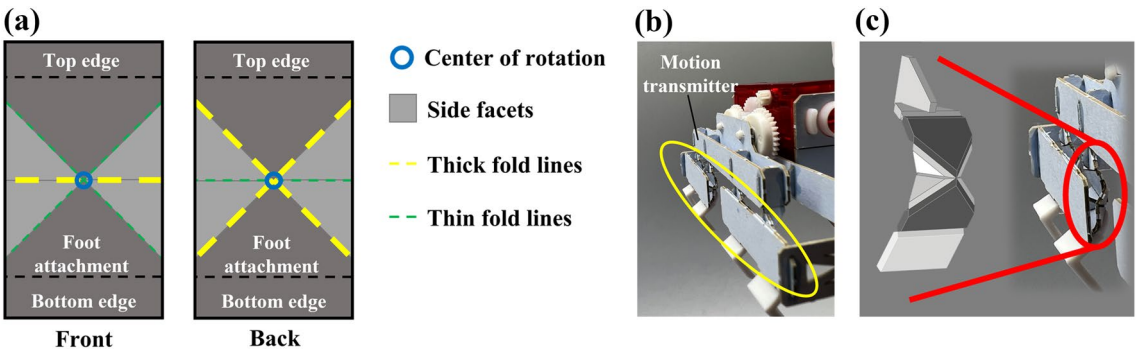

Fig. 3 **a** The 2D pattern of the spherical six-bar linkage. All fold lines, the axis of the joints, meet at the center of rotation. **b** and **c** show how the spherical six-bar is installed on the crawler

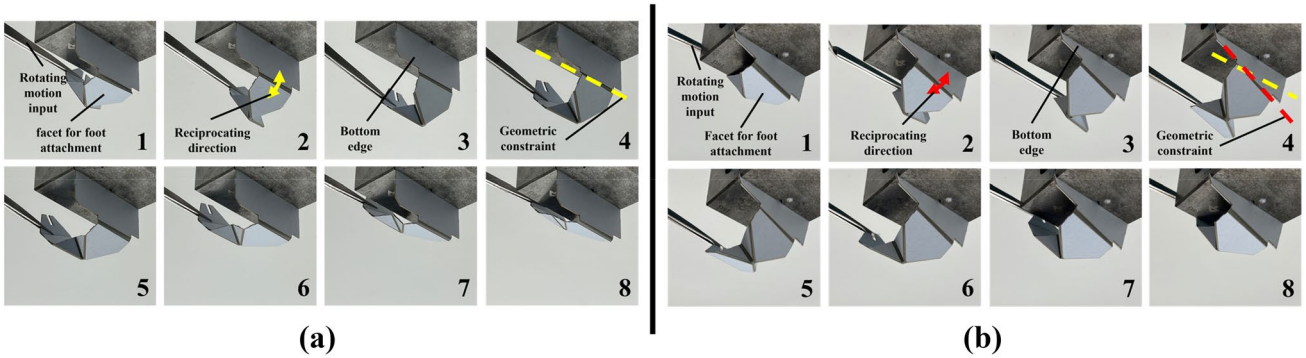

Fig. 4 The working process of the constrained spherical six-bar. **a** is when the constrained angle is 0°. **b** is when the constrained angle is given and the direction of the reciprocating motion changes accordingly

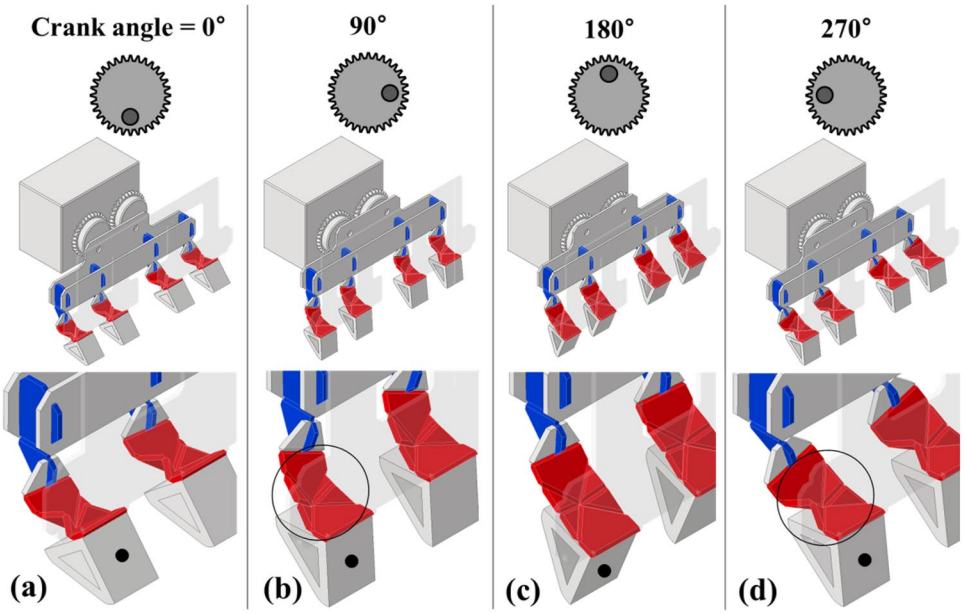

Fig. 5 How to transfer the rotary motion of the crank to the reciprocating motion of the rear crawling legs. The asymmetric folding of the spherical six-bar is shown in **b** and **c**, which passes only the reciprocating motion to the crawling legs

Fig. 5d. Like the situation in Fig. 5b, the side facets of the spherical six-bar filter the up-and-down motion by being asymmetrically folded.

2.2 Steering Mechanism

Steering ability is essential for crawling robots to reach where they plan to go. The OriSCO achieves steering by changing the direction of the propulsion force. Since spherical six-bar linkage is capable of generating both pitch and yaw motion when driving [23], this is done by changing the constrained angle of the spherical six-bar linkage as shown in Fig. 4. The direction of reciprocation, indicated by the yellow arrow in Fig. 4(a-2), varies depending on the angle of the bottom edge. When the angle of the bottom edge, the geometric constraint, changes as shown in Fig. 4(b-4), the reciprocating direction changes as well as indicated in Fig. 4(b-2). Using this property, the kicking direction of the crawling legs can be controlled, and this finally enables us to give the OriSCO a steering capability.

In order to change the constrained angle of the spherical six-bar, a servo motor is used. The servo motor is attached to the top of the gearbox and the end effector of the servo motion is connected to a steering bar as shown in Fig. 1b. The role of the steering bar is to give a distortion to the hip joint, which is operated by the servo motor. Figure 6 shows the detailed process of how to change the constrained angle of the spherical six-bar by tilting the steering bar.

Figure 6a, b is when the steering bar is in neutral position. Figure 6a, b shows the crawling legs and the steering axis, indicated by the blue dashed line, is in the upright position as well. In other words, the blue dashed line indicates the

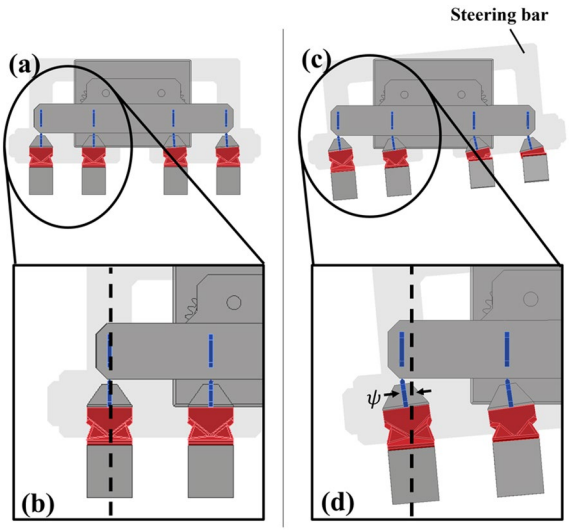

Fig. 6 The steering process. **a** and **b** are when the constrained angle of the spherical six-bar is 0°. In **c** and **d**, the steering bar is inclined and accordingly, the constrained angle has an angle of ψ

reciprocating direction of the crawling legs. In neutral position, therefore, the crawler receives propulsive force in the forward direction. Figure 6c, d are when the steering bar is in the position to move to the left. The steering bar is tilted by the servo motor, and accordingly, the steering axis has the angle ψ, as shown in Fig. 6d. Due to the inclined steering axis, the reciprocating direction of the legs also changes, and finally the crawler gets propulsion to move to the left.

2.3 Fabrication

This process adopts the SCM manufacturing method, and the overall process is shown in Fig. 7a. The fabrication process starts with attaching the paper board with the thermal adhesive using a heating roller. The paper board has a thickness of 740 µm (without fabric) and 850 µm (with fabric). The attached materials and the fabric are then processed with the laser system, which allows meticulous machining, and subsequently the materials are laminated according to the order as shown in Fig. 7a.

The OriSCO is assembled via a folding process. Figure 7b, c shows the laser-cut development figure. The alignment holes at the edges are used when laminating the paper and fabric to prevent dislocation between the materials [24], and separating the parts by cutting off the gates and gluing the parts. The prerequisite process, which is from cutting the paper to combining the board and adhesive, takes 4 min, and the laser cutting process takes 37 min. Removing the gates takes 11 min, and the gluing process takes 17 min.

2.4 Other Components

The components of the OriSCO are arranged in four large groups: paperboard parts, plastic feet, an actuator, and a gear. The plastic feet are 3D printed with ABS plastic using Cubicon Single Plus. The steering actuator is a servo motor (Tower Pro SG90). The gear box has two DC motors (6 mm diameter, DRC mall). One for the front legs and one for the rear legs. In addition, a 180 mA h lithium polymer battery and gear shafts are included. The OriSCO is controlled by infrared (IR) communication. The total mass budget of the OriSCO is given in Table 1.

Table 1 The mass budget table for octopod components

Components	Mass per part (g)	Number of parts	Ratio to overall mass (%)
Paperboard parts	7.51	20	16.03
Horn holder	0.23	1	0.49
Plastic toe (Front)	0.20	4	1.69
Plastic toe (Rear)	0.30	4	2.55
Servo motor	10.26	1	21.90
Gearbox	26.88	1	57.36
Total	46.86	–	100

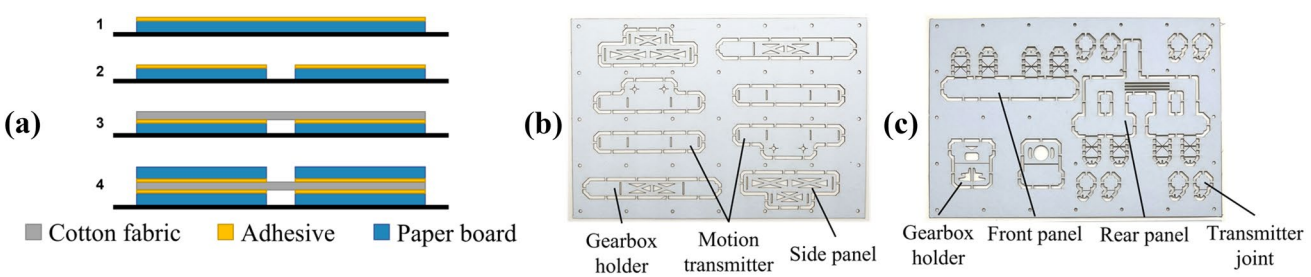

Fig. 7 **a** The process of smart composite microstructures (SCM). **b** and **c** are the planar state after SCM manufacturing. **b** is for the body structure and **c** is for the steering bar and the crawling legs

3 Modeling and Analysis

Since the constrained spherical six-bar linkage plays a pivotal role in this research, a kinematic model should be suggested to check whether the linkage is functioning properly as a mechanical filter or not. Through the kinematic model, the shape of the leg trajectory is investigated quantitatively.

Moreover, as previously stated, the reciprocating direction of the crawling legs varies depending on the constrained angle of the spherical six-bar linkage, which allows the crawler to have steering ability. This phenomenon is also modeled kinematically to observe the change of the leg trajectory by varying the constrained angle.

3.1 Spherical Six-bar Kinematics

The schematic of the kinematic model is shown in Fig. 8a when the constrained angle is zero. The kinematics is analyzed based on the 3-dimensional vector loop as follows:

$$\vec{r} + \vec{L}_3 + \vec{L}_2 + \vec{L}_1 = \vec{G} \tag{1}$$

$$r\begin{bmatrix}\cos\theta_1\\ \sin\theta_1\\ 0\end{bmatrix} + L_3\begin{bmatrix}\cos\theta_2\\ \sin\theta_2\\ 0\end{bmatrix} + L_2\begin{bmatrix}\sin\phi_3\cos\theta_2\\ \sin\phi_3\sin\theta_2\\ \cos\phi_3\end{bmatrix} + L_1\begin{bmatrix}\sin\phi_4\\ 0\\ \cos\phi_4\end{bmatrix} = \begin{bmatrix}G\\ 0\\ -d\end{bmatrix}, \tag{2}$$

where r is the radius of the crank, L_1 is the linkage connected to the crank, L_2 is the six-bar part near the crank, L_1 is the six-bar connected to the outer panel, G is the distance between the center of the crank and the L_1 joint, and d is the distance between the crank frame and the outer frame.

Figure 8b shows how the crawling legs move while the crank rotates a single revolution.

However, when the constrained angle changes, the trajectory of the six-bar also changes. Figure 8c indicates the schematic when the constrained angle has a specific angle. It can be analyzed using the 3D vector loop as follows:

$$r\begin{bmatrix}\cos\theta_1\\ \sin\theta_1\\ 0\end{bmatrix} + L_3\begin{bmatrix}\cos(\theta_2+\psi)\\ \sin(\theta_2+\psi)\\ 0\end{bmatrix} + L_2\begin{bmatrix}\sin\phi_3\cos(\theta_2+\psi)\\ \sin\phi_3\sin(\theta_2+\psi)\\ \cos\phi_3\end{bmatrix} + L_1\begin{bmatrix}\sin\phi_4\cos\psi\\ \sin\phi_4\sin\psi\\ \cos\phi_4\end{bmatrix} = \begin{bmatrix}G\cos\psi\\ G\sin\psi\\ -d\end{bmatrix}, \tag{3}$$

where ψ is the constrained angle along y-axis.

Figure 8d shows how the crawling legs move while the crank rotates a single revolution.

3.2 Leg Trajectory Analysis

The toe trajectory of the robot changes on the coronal plane in the left and right diagonal. The trajectory difference along the angle difference is depicted in Fig. 9.

Figure 9 shows the leg trajectories by varying the constrained angle of the spherical six-bar linkage. Since the constrained angle ψ is included in the vector array of the

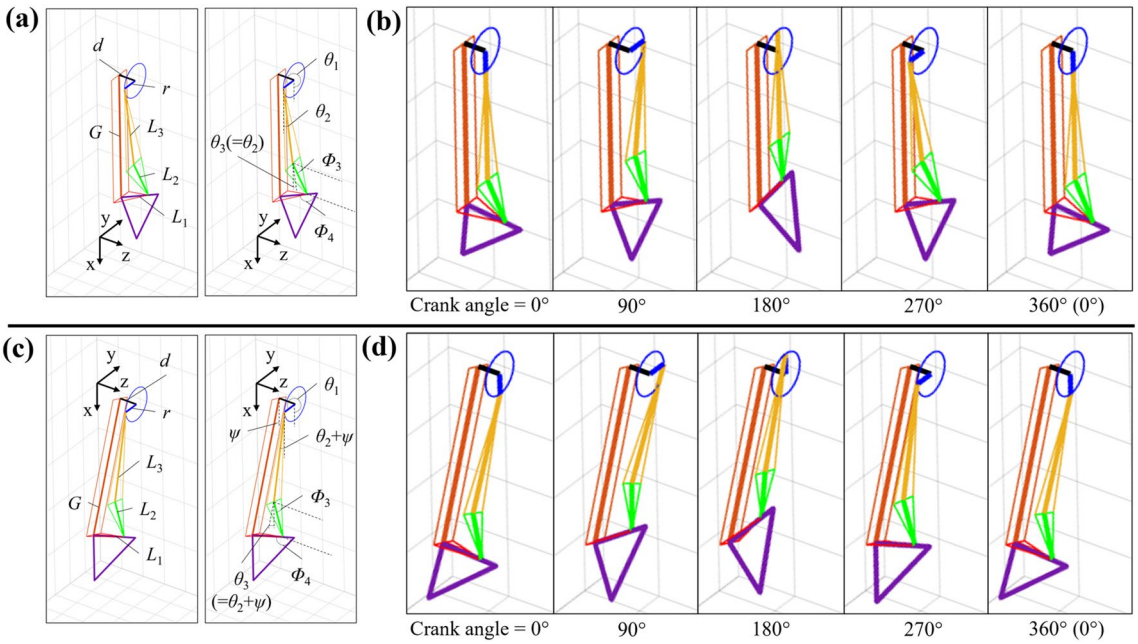

Fig. 8 **a** and **b** are the schematics when the constrained angle is 0° and 20°, respectively

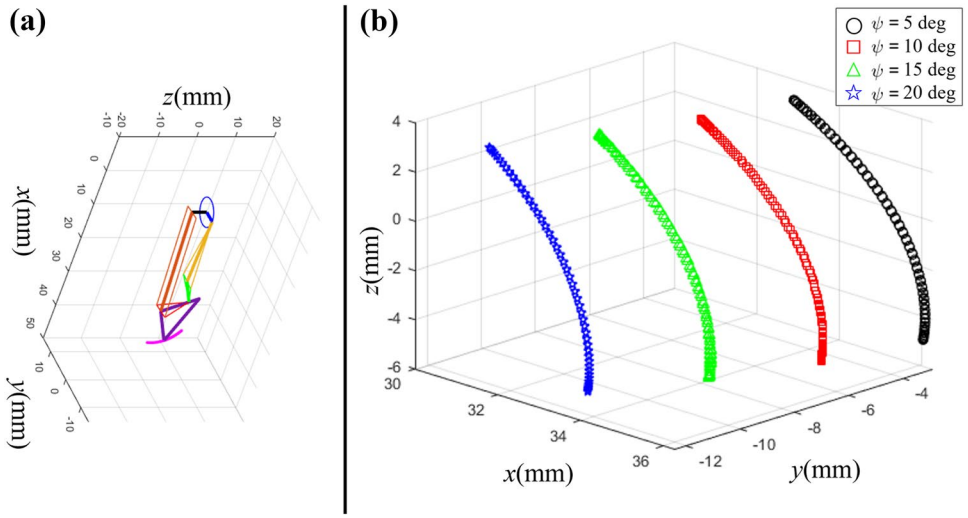

Fig. 9 The difference of the foot trajectory with respect to the constrained angle, ψ. **a** The schematic of a single spherical six-bar linkage system and the toe. **b** The trajectories of the toe end depending on the constrained angle

linkages L_1, L_2, L_3, and G, the toe trajectory varies when the constrained angle of the steering bar changes. If the constraint angle is in an idle state—no angle change on the steering bar—the trajectory is parallel to the sagittal plane. When the steering bar is in a directional state—when there are angle changes on the steering bar—the trajectory is represented in a left and right diagonal with respect to the sagittal plane. It thereby means that the crawler can steer itself toward left and right.

The degree of trajectory change depends on the constraint angle ψ, as shown in Fig. 9. In the analysis, a larger ψ shows a more slanted trajectory, which would imply a larger turning angle. However, due to the limited flexibility of the steering bar, the range of ψ is limited to ± 10 degrees from the neutral position based on the empirical decision.

4 Experimental Results

Two experiments are carried out to validate the proposed concept. The first is to investigate the direction of the propulsion force depending on the constrained angle. This will tell us whether steering can be achieved by controlling the constrained angle using a servomotor.

In addition, crawling performance such as speed and steering ability are investigated based on video analysis. A high-speed camera is used to observe the crawling motion at a frame rate of 1000 fps. Reaction forces in the vertical direction and the horizontal direction are also measured. By analyzing the reaction forces, the role of the front legs and hind legs is examined to see if they are working properly as we intended.

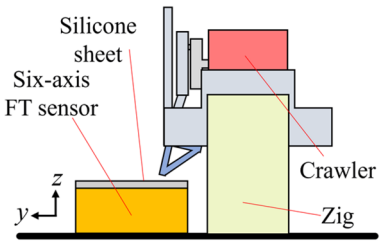

Fig. 10 The experimental setup for measuring the propulsion force in x, y, and z directions. A six-axis force-torque (FT) sensor (RFT40-SA01, Robotous Inc.) is used to measure ground reaction forces, and a silicone film is attached to the top of the sensor to prevent slippage

4.1 Direction of Propulsion Force

In the simulated results in Fig. 9b, the toe trajectory varies depending on the constrained angle, ψ. In other words, the toe trajectory can be controlled by adjusting the constrained angle. If we want to control the direction of propulsion force through the constrained angle as well, we need to check whether the toe trajectory is aligned with the direction of propulsion force. To this end, in Fig. 10, an experimental setup is made to measure the direction of the propulsion forces while varying the constrained angle of the spherical six-bar.

Figure 11 shows the directions of the measured forces and the simulated toe trajectories depending on the angle of constraint. The force directions represent the average of ten measured strokes for each degree. Only the directions of the forces are plotted—the magnitude of the force

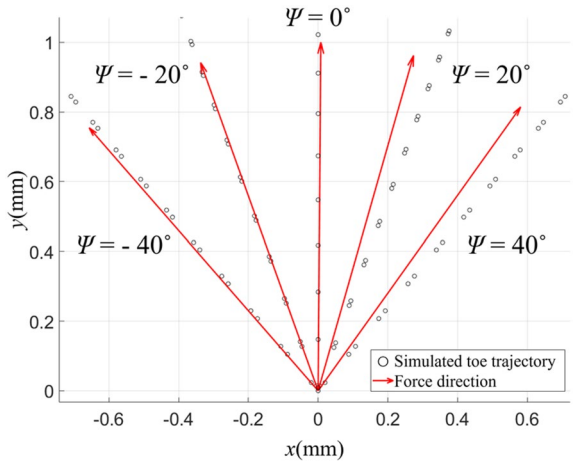

Fig. 11 The simulated trajectories of a toe and the corresponding experimental force directions with respect to the constrained angle, ψ

vector is normalized—since the magnitude varies depending on the distance between the FT sensor and the toe of the crawler. In Fig. 11, there is a slight difference in the toe trajectory and drive force when the constrained angle is − 40°, 20°, and 40°. This error may be due to joint compliance. A fabric material is used to manufacture the joint, and wrinkles may occur against the external force, which may affect the movement of the toe. Overall, however, the direction of the propulsion forces seems to be well aligned with the toe trajectories. From this result, it can be said that the direction of the propulsion force can be controlled by adjusting the constrained spherical six-bar linkage.

4.2 Crawling Performance

To check whether the crawler is actually able to steer, the position data are plotted as the crawler moves forward, left, and right, as shown in Fig. 12a. The markers in Fig. 12a are indicated every 66 ms.

In the case of forward crawling, the black colored markers in Fig. 12a look nearly straight. This can be confirmed by the velocity data in Fig. 12b. The crawling velocity in *y*-direction shows 116.23 mm/s on average, while the velocity in *x*-direction is 2.50 mm/s.

When it comes to turning, the red and blue colored markers represent left and right turning, respectively, as shown in Fig. 12a. The data are plotted while the crawler is turning 180 degrees. In the case of the left turn, the turning radius is measured to be 47.54 mm and the turning speed is indicated to be 91.93 deg/s. Figure 12c shows the velocity of the crawler during the left turn. The velocity in *y*-direction decreases to zero and finally reaches − 137.7 mm/s. In *x*-direction, the velocity decreases to − 123.93 mm/s and increases again to zero.

The right turn in Fig. 12a has a turning radius of 20.56 mm and a turning speed of 60.73 deg/s. The velocity data are given in Fig. 12d and shows the opposite trend to that of the left turn. The velocity in x-direction increases to 83.76 mm/s and decreases to zero. In the y-direction, the velocity decreases to zero and ends up at − 68.85 mm/s.

4.3 Reaction Force While Crawling

Examining ground reaction force helps describe the kinematics and forces during locomotion [25]. Moreover, leg

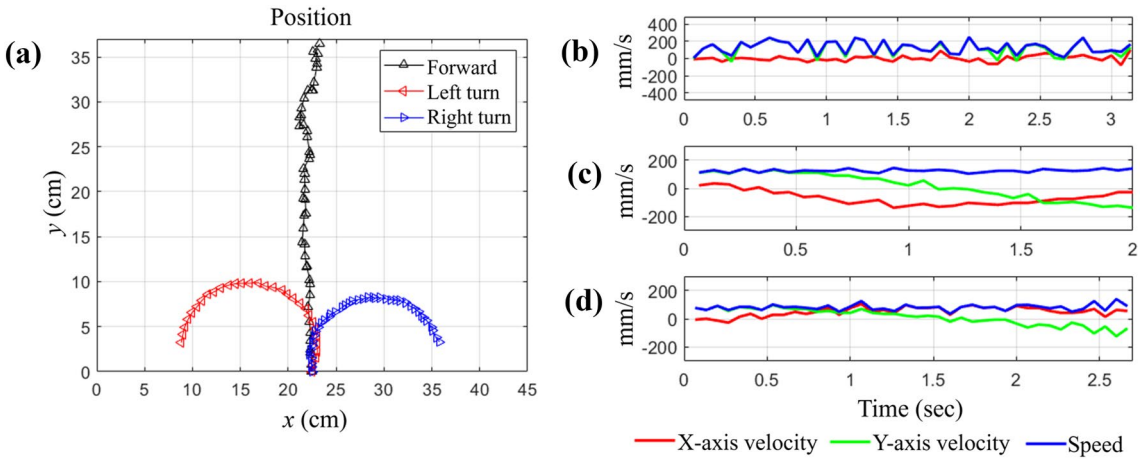

Fig. 12 **a** The position data when the crawler moves forward, left and right. The turning data are collected while the crawler achieves the turning angle of 180°. **b**, **c** and **d** are the forward, left and right turning speeds, respectively. The red and green lines represent the velocity along the *x* and *y* axes, respectively, and the blue lines show the sum of the *x* and *y* speed, which represents the speed in the forward direction

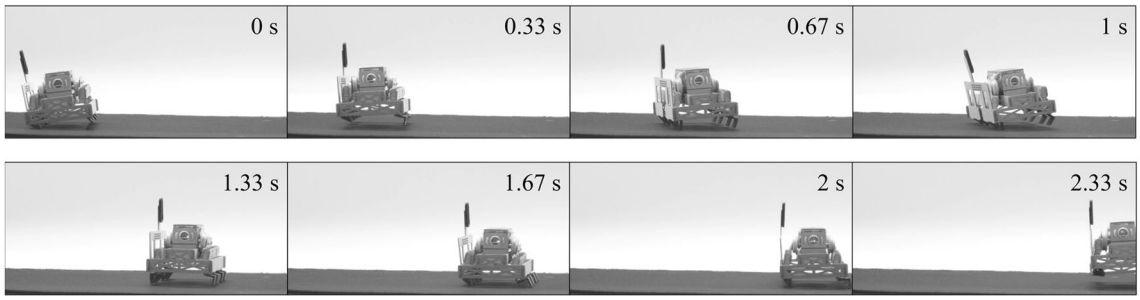

Fig. 13 High-speed images during forward crawling. The images are taken with the frame rate of 900 fps

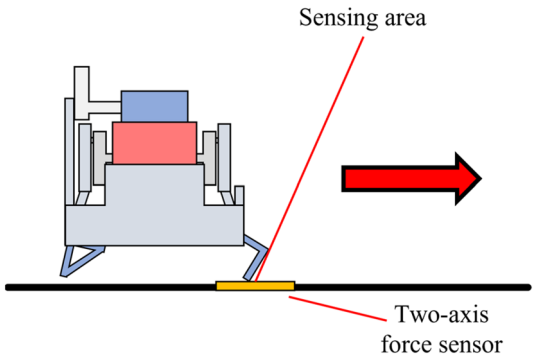

Fig. 14 Experimental setup to measure the reaction force in the vertical and the horizontal directions

mechanism must consume the energy in the direction of gravity as well as in the propulsive direction of the body [26]. In this manner, for successful crawling, the crawling legs of the OriSCO are designed to have their own roles. The front legs kick the ground vertically and lift the body into the air to minimize friction. Simultaneously, the rear legs kick the ground horizontally and propel the body forward. Thanks to this strategic design, the OriSCO achieves the crawling motion shown in Fig. 13.

To investigate whether the crawling legs are working properly, the reaction force during crawling is measured. Figure 14 shows the experimental setup. To measure the vertical and horizontal forces simultaneously, a dual-axis load cell is used and the data are collected at a sampling frequency of 950 Hz.

Figure 15a, b is the measured reaction force of the front leg and rear leg, respectively. If we compare the vertical reaction force, the front leg has about 270 mN more force than the rear leg. In the case of horizontal force, the rear leg has more force compared to the front leg. In summary, the front leg has high vertical force and low horizontal force, while the rear leg has relatively lower vertical force and higher horizontal force compared to the front leg. Based on this observation, it is estimated that the crawling legs are working properly as we designed them.

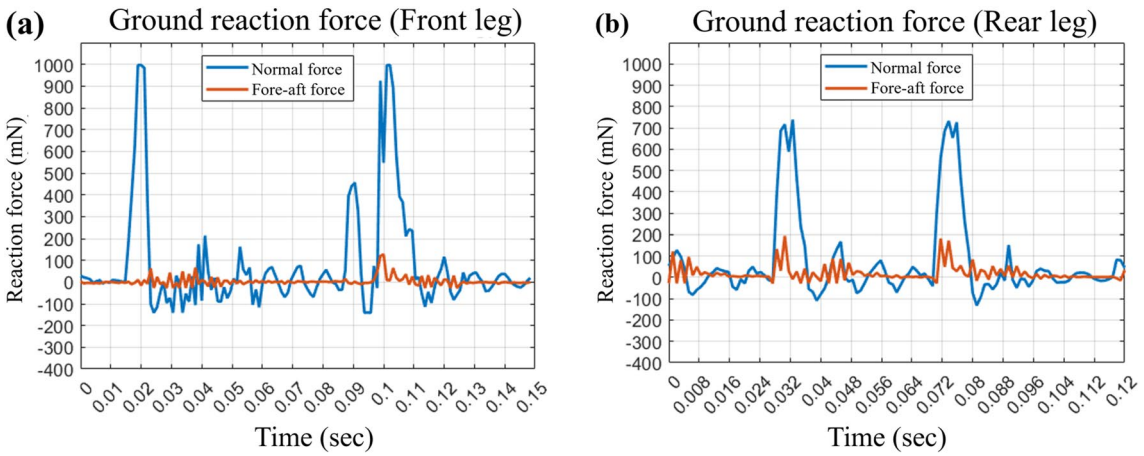

Fig. 15 Ground reaction force during forward crawling. The vertical reaction force and the horizontal reaction force of (**a**) the front leg and (**b**) the rear leg

5 Conclusion

In this paper, a novel steering method for milli-scale crawling robots is proposed. Two design strategies are used: the constrained spherical six-bar linkage and the active control of the constrained angle. The constrained spherical six-bar linkage works as a mechanical filter that transfers the rotary motion of the motor to the reciprocating motion of the crawling legs. Active control of the constrained angle determines the direction of the reciprocating motion, allowing the direction of the propulsion force to be changed as well. This steering concept is applied to a crawling robot called OriSCO. By applying the design strategies, the OriSCO successfully crawls, steers, and reaches where the robot plans to go.

Acknowledgements This work was supported by the Research Program funded by the SeoulTech (Seoul National University of Science and Technology).

Funding Seoultech.

Data Availability The datasets generated during and/or analyzed during the current study are available from the corresponding author on reasonable request.

Declarations

Conflict of Interest On behalf of all the authors, the corresponding author states that there is no conflict of interest.

References

1. Song, X. G., Pan, J. J., Lin, F. M., Zhang, X. L., Chen, C. J., & Huang, D. S. (2022). Cockroach-inspired traversing narrow obstacles for a sprawled hexapod robot. *Journal of Bionic Engineering, 19*(5), 1288–1301.
2. Hoover, A. M., Burden, S., Fu, X. Y., Sastry, S. S., & Fearing, R. S. (2010). Bio-inspired design and dynamic maneuverability of a minimally actuated six-legged robot. *In Proceedings of the 2010 3rd IEEE RAS & EMBS International Conference on Biomedical Robotics and Biomechatronics*, Tokyo, Japan, 869–876.
3. Ding, X. L., & Yang, F. (2016). Study on hexapod robot manipulation using legs. *Robotica, 34*(2), 468–481.
4. Kohut, N. J., Pullin, A. O., Haldane, D. W., Zarrouk, D., & Fearing, R. S. (2013). Precise dynamic turning of a 10 cm legged robot on a low friction surface using a tail. *In Proceedings of the 2013 IEEE International Conference on Robotics and Automation*, Karlsruhe, Germany, 3299–3306.
5. Baisch, A. T., Sreetharan, P. S., & Wood, R. J. (2010). Biologically-inspired locomotion of a 2g hexapod robot. *In Proceedings of the 2010 IEEE/RSJ International Conference on Intelligent Robots and Systems*, Taipei, Taiwan, 5360–5365.
6. Qu, J. H., Choi, J. S., & Oldham, K. R. (2017). Dynamics of millimeter-scale hexapod microrobotics with PZT-polymer microactuators. *In Proceedings of the 2017 IEEE International Conference on Advanced Intelligent Mechatronics* (AIM), Munich, Germany, 1304–1309.
7. Hoover, A. M., Steltz, E., & Fearing, R. S. (2008). RoACH: An autonomous 2.4 g crawling hexapod robot. *In Proceedings of the 2008 IEEE/RSJ International Conference on Intelligent Robots and Systems*, Nice, France, 2008, 26–33.
8. Haldane, D. W., Peterson, K. C., Bermudez, F. L. G., & Fearing, R. S. (2013). Animal-inspired design and aerodynamic stabilization of a hexapedal millirobot. *In Proceedings of the IEEE International Conference on the Robotics and Automation*, Karlsruhe, Germany, 2013, 3279–3286.
9. Pullin, A. O., Kohut, N. J., Zarrouk, D., & Fearing, R. S. (2012). Dynamic turning of 13 cm robot comparing tail and differential drive. *In Proceedings of the IEEE International Conference on the Robotics and Automation*, Saint Paul, MN, USA, 2012, 5086–5093.
10. Hoffman, K. L., & Wood, R. J. (2011). Passive undulatory gaits enhance walking in a myriapod millirobot. *In Proceedings of the IEEE/RSJ International Conference on Intelligent Robots and Systems*, San Francisco, CA, USA, 2011, 1479–1486.
11. Baisch, A. T., Heimlich, C., Karpelson, M., & Wood, R. J. (2011). HAMR3: An autonomous 1.7 g ambulatory robot. *In Proceedings of the IEEE/RSJ International Conference on Intelligent Robots and Systems*, San Francisco, CA, USA, 2011, 5073–5079.
12. Soltero, D. E., Julian, B. J., Onal, C. D., & Rus, D. (2013). A lightweight modular 12-dof print-and-fold hexapod. *In Proceedings of the IEEE/RSJ International Conference on Intelligent Robots and Systems*, Tokyo, Japan, 2013, 1465–1471.
13. Kim, T. Y., Kim, C., Kim, S. H., & Jung, G. P. (2019). MutBug: A lightweight and compact crawling robot that can run on both sides. *IEEE Robotics and Automation Letters, 4*(2), 1409–1415.
14. Lee, J., Jung, G. P., Baek, S. M., Chae, S. H., Yim, S., Kim, W., & Cho, K. J. (2020). CaseCrawler: A lightweight and low-profile crawling phone case robot. *IEEE Robotics and Automation Letters, 5*(4), 5858–5865.
15. Birkmeyer, P., Peterson, K., & Fearing, R. S. (2009). DASH: A dynamic 16g hexapedal robot. *In Proceedings of the IEEE/RSJ International Conference on Intelligent Robots and Systems*, St. Louis, MO, USA, 2009, 2683–2689.
16. Felton, S., Tolley, M., Demaine, E., Rus, D., & Wood, R. (2014). A method for building self-folding machines. *Science, 345*(6197), 644–646.
17. Goldberg, B., Zufferey, R., Doshi, N., Helbling, E. F., Whittredge, G., Kovac, M., & Wood, R. J. (2018). Power and control autonomy for high-speed locomotion with an insect-scale legged robot. *IEEE Robotics and Automation Letters, 3*(2), 987–993.
18. Sahai, R., Avadhanula, S., Groff, R., Steltz, E., Wood, R., & Fearing, R. S. (2006). Towards a 3g crawling robot through the integration of microrobot technologies. *In Proceedings of the IEEE International Conference on the Robotics and Automation*, Orlando, FL, USA, 296–302.
19. Schilling, M., Hoinville, T., Schmitz, J., & Cruse, H. (2013). Walknet, a bio-inspired controller for hexapod walking. *Biological cybernetics, 107*, 397–419.
20. Su, M. J., Xie, R. Z., Qiu, Y., & Guan, Y. S. (2023). Design, mobility analysis and gait planning of a leech-like soft crawling robot with stretching and bending deformation. *Journal of Bionic Engineering, 20*(1), 69–80.
21. Wood, R. J., Avadhanula, S., Sahai, R., Steltz, E., & Fearing, R. S. (2008). Microrobot design using fiber reinforced composites. *ASME Journal of Mechanical Design, 130*(5), 052304.
22. Koh, J. S., & Cho, K. J. (2012). Omega-shaped inchworm-inspired crawling robot with large-index-and-pitch (LIP) SMA spring actuators. *IEEE/ASME Transactions on Mechatronics, 18*(2), 419–429.

23. Chen, S. E., Cao, Y. T., Sarparast, M., Yuan, H. Y., Dong, L. X., Tan, X. B., & Cao, C. Y. (2020). Soft crawling robots: Design, actuation, and locomotion. *Advanced Materials Technologies, 5*(2), 1900837.
24. Bae, S. Y., Koh, J. S., & Jung, G. P. (2021). A miniature flapping mechanism using an origami-based spherical six-bar pattern. *Applied Science, 11*(4), 1515.
25. Wöhrl, T., Reinhardt, L., & Blickhan, R. (2017). Propulsion in hexapod locomotion: How do desert ants traverse slopes? *Journal of Experimental Biology, 220*(9), 1618–1625.
26. Kobayashi, H., & Inagaki, K. (1991). Development of a hexapod walking robot:'Hexax-I'. *In Proceedings of the IROS'91: IEEE/RSJ International Workshop on Intelligent Robots and Systems' 91*, Osaka, Japan, 1991, 1545–1549.